ASCE

Temporal Evaluation of ASR Cracking in Concrete Specimens Using Acoustic Emission

Vafa Soltangharaei, M.ASCE[1]; Rafal Anay[2]; Li Ai[3]; Eric R. Giannini, M.ASCE[4]; Jinying Zhu[5]; and Paul Ziehl, M.ASCE[6]

Abstract: The effect of steel reinforcement on the distribution of alkali-silica reaction (ASR) damage in concrete blocks is studied by leveraging acoustic emission sensing with a data-driven approach. The innovation lies in deriving damage contours caused by ASR based on a minimal sensor array. Through this approach, damage progression can be traced in time and event distribution can be visualized. A gap in the current literature, namely evaluating ASR progress in concrete structures with different internal restraint using acoustic emission (AE), is addressed. Unsupervised pattern recognition is utilized to study the effect of the temporal damage condition. In the confined specimen, the distribution of AE events in the midwidth region of the specimen is concentrated and close to the normal distribution. The surface cracks are mostly oriented along the specimen length and in the midwidth region. However, in the unconfined specimen, the distribution of AE events is more uniform, and cracks are randomly distributed. **DOI: 10.1061/(ASCE)MT.1943-5533.0003353.** © *2020 American Society of Civil Engineers.*

Author keywords: Acoustic emission (AE); Alkali-silica reaction (ASR); Damage imaging; Unsupervised pattern recognition.

Introduction

Alkali-silica reaction (ASR) is one source of damage in concrete structures. The reaction occurs between the alkali hydroxides (NaOH, KOH) in the pore solution, mainly from the cement, and certain siliceous minerals present in some concrete aggregates (Barbosa et al. 2018; Rajabipour et al. 2015; Villeneuve et al. 2012). The result of the reaction is a hygroscopic alkali-silica gel that tends to absorb water and expand. The reaction and subsequent swelling are accelerated by high temperatures and humidity over approximately 80%. The gel expands and exerts pressure on the cement matrix and aggregates (Garcia-Diaz et al. 2006). This pressure causes microcracks and macrocracks in the concrete components. Different structures have been affected by ASR such as concrete dams (Blanco et al. 2019; Campos et al. 2018; Plusquellec et al. 2018), bridges (Barbosa et al. 2018; Lahdensivu et al. 2018; Schmidt et al. 2014), and nuclear structures (nuclear power plants and nuclear waste containments) (Hariri-Ardebili and Saouma 2018; Saouma and Hariri-Ardebili 2014; Soltangharaei et al. 2018; Tcherner and Aziz 2009).

Several methods have been used for monitoring ASR progress in structures. Some common methods include visual inspection, coring (Barbosa et al. 2018; Islam and Ghafoori 2018), petrographic analysis, including the Damage Rating Index (DRI) (Abdelrahman et al. 2015; Barbosa et al. 2018; Rivard and Ballivy 2005; Rivard et al. 2010; Sanchez et al. 2015, 2020; Taylor et al. 2012), demountable mechanical strain gauges (DEMEC gauge) (Allard et al. 2018; Hayes et al. 2018; Sinno and Shehata 2019), relative humidity or moisture content measurement, and crack indexing (Hayes et al. 2018; Thomas et al. 2013). Despite the simplicity of these methods, they have some drawbacks. For instance, visual inspection is not efficient for the early detection of ASR damage because ASR damage initiates internally in the concrete and then extends to the surface. This is more critical in thick shear walls (e.g., nuclear structures), where most of the expansion happens out-of-plane due to in-plane confinement and the damage on the surface appears in the latter stages of the ASR reaction. Furthermore, visual inspection is time-consuming and often operator-dependent, especially for large-scale structures, although advances in drone inspection and image analysis could improve visual inspection (Seo et al. 2018; Yang et al. 2015; Zink and Lovelace 2015). Crack indexing is also time-consuming and not easily applied for evaluating very large and complex structures. Although DEMEC gauges are generally useful for some structural components such as piles and columns, it is not a well-suited index for studying damage in shear walls, because it measures expansion on the surface rather than through the thickness. Petrography is helpful for ASR damage quantification using a damage rating index, but it is time-consuming and intrusive. In addition, the method is focused on microscale damage in the concrete and diagnosing the cause(s) of distress, but it is difficult to generalize petrography results for the structural capacity. Coring is also a destructive method, and large numbers of cores are impractical for potentially sensitive structures such as nuclear containments.

Nondestructive methods (Giannini et al. 2013; Mahadevan et al. 2016) are an alternative for damage quantification and

[1]Graduate Research Assistant, Dept. of Civil and Environmental Engineering, Univ. of South Carolina, Columbia, SC 29208. Email: vafa@email.sc.edu

[2]Postdoctoral Fellow, Dept. of Civil and Environmental Engineering, Univ. of South Carolina, Columbia, SC 29208. Email: ranay@email.sc.edu

[3]Graduate Research Assistant, Dept. of Civil and Environmental Engineering, Univ. of South Carolina, Columbia, SC 29208. Email: ail@email.sc.edu

[4]Principal Investigator, RJ Lee Group, Monroeville, PA 15146. ORCID: https://orcid.org/0000-0003-3938-3478. Email: egiannini@rjleegroup.com

[5]Associate Professor, College of Engineering, Civil Engineering, Univ. of Nebraska-Lincoln, Lincoln, NE 68588-0531. Email: jyzhu@unl.edu

[6]Professor, Dept. of Civil and Environmental Engineering, Univ. of South Carolina, Columbia, SC 29208 (corresponding author). ORCID: https://orcid.org/0000-0002-4783-9255. Email: ziehl@cec.sc.edu

Note. This manuscript was submitted on September 18, 2019; approved on March 5, 2020; published online on July 25, 2020. Discussion period open until December 25, 2020; separate discussions must be submitted for individual papers. This paper is part of the ***Journal of Materials in Civil Engineering***, © ASCE, ISSN 0899-1561.

condition assessment of structures affected by ASR. Several methods have been employed for this purpose such as digital image correlation (Teramoto et al. 2018), nonlinear Rayleigh surface ultrasonic (Kim et al. 2018; Lokajíček et al. 2017), ultrasonic pulse velocity (Rivard and Saint-Pierre 2009), dynamic modulus of elasticity (Sargolzahi et al. 2010), impact-echo (Giannini et al. 2013), and acoustic emission (AE) (Abdelrahman et al. 2015; Farnam et al. 2015; Lokajíček et al. 2017; Pour-Ghaz et al. 2012; Soltangharaei et al. 2018; Weise et al. 2012). AE is a passive structural health monitoring approach that has recently been utilized for detection of damage in concrete elements. This method uses piezoelectric sensors to respond to elastic stress waves emitted by crack formation and records them as digital signals, usually amplified through external or integral preamplifiers. The sensors are very sensitive and can capture internal microscale damage development. Furthermore, AE can monitor structural condition continuously without disrupting use of the structure, damage localization is feasible, and the method is applicable when only one side of the structure is accessible.

To date, AE has mainly been explored for small-scale concrete specimens affected by ASR without steel reinforcement. For example, Pour-Ghaz et al. (2012) employed AE to monitor the cracking in addition to expansion measurement in cylindrical mortar specimens with lengths of 28 and 36 cm and different diameters ranged 2.5–10.2 cm. They found that AE was able to detect ASR cracking earlier than the occurrence of significant length change (0.1%). Moreover, they observed a decrease in the cumulative energy in the later stage of the experiment, which was related to an increase of attenuation due to cracking or ASR gel in the specimens. Abdelrahman et al. (2015) found a correlation between AE cumulative signal strength and expansion from ASR measured per ASTM C1293 (ASTM 2020). Furthermore, parameters of intensity analysis were correlated with the petrographic damage rating index (DRI). Farnam et al. (2015) used mortar cylinders with a diameter and height of 20 and 40 mm. AE signals were characterized according to peak frequency and frequency centroid, and high-frequency signals were related to microcracking in aggregates. Lokajíček et al. (2017) utilized AE to monitor ASR in mortar prisms with different aggregate reactivities and reported a correlation between cumulative AE energy and damage.

In these prior works, small-scale specimens were mostly investigated without any internal or external confinement. However, in reality, structures have different internal or external restraints, and it has been shown that restraints have a significant effect on damage distribution due to ASR (Allard et al. 2018; Barbosa et al. 2018; Gorga et al. 2018; Karthik et al. 2016; Liaudat et al. 2018; Morenon et al. 2017; Saouma et al. 2016). Soltangharaei et al. (2018) utilized internal broadband sensors to monitor the ASR cracking for large-scale specimens. The effect of external confinemet on the ASR expansion and AE data has been studied.

In the current study, a large number of sensors (compared to the volume of concrete) are utilized in the medium-scale specimens, which facilitates source localization. A new procedure is developed to visualize the temporal development of ASR damage in concrete structures using AE. AE event distributions are derived and compared with surface crack patterns, crack widths, and petrography results, which provide more insight into ASR cracking. The authors are not aware of investigation reported in the open literature to virtualize the temporal development of ASR damage using AE. Furthermore, the effect of longitudinal and transverse reinforcement on damage distribution and progression in terms of AE data is addressed in this paper. Three medium-scale specimens with and without reinforcements were cast and prepared for accelerated aging. AE was continuously monitored and expansion strains and crack width intermittently measured. Petrographic analysis was conducted at the end of the experiment. Correlations between expansion, crack width data, and petrographic analysis to the AE data are discussed.

Test Setup and Procedure

Three concrete block specimens with dimensions $305 \times 305 \times 1{,}120$ mm were cast at the University of Alabama and delivered to the University of South Carolina for testing. The sensor layouts, geometries, and structural details are presented in Fig. 1. Two specimens were cast with reactive coarse aggregates and the third had nonreactive aggregate to serve as a control specimen. Only coarse aggregates were reactive. One of the reactive specimens had reinforcing steel along two dimensions (X and Z). This specimen is referred to as the confined specimen in this paper. The other reactive specimen did not have any reinforcement. This specimen is referred to as the unconfined specimen in this paper. The reinforcement details for the confined specimen is presented in Fig. 1(b). The confined specimen had four longitudinal US #7 steel rebars and US #6 steel rebars at 150 mm on the center as transverse reinforcement [Fig. 1(b)]. All rebars were T-headed to compensate for the short development length. The specimen without reactive aggregate is referred to as the control specimen. It did not have any steel reinforcement like the unconfined specimen as shown in Fig. 1(d).

Ten acoustic emission sensors were affixed to the surfaces of each reactive specimen (confined and unconfined specimens) as illustrated in Fig. 1(a), and four sensors were attached to the surfaces of the control spcecimen Fig. 1(c). All sensors were wideband type PKWDI with 26-dB internal preamplification. The frequency operating range of the sensors is 200–850 kHz. The sensitivity curve of PKWDI can be found in MISTRAS Group (2011). The sensor coordinates are presented in Table 1. The table has two sections separated by a vertical line, which includes the sensor locations of the confined and unconfined specimens and the sensor locations of the control specimen. Some sensor locations were indicated in Figs. 1(a and c). Sensors 1 and 2 are located on the top surfaces of the reactive specimens. Sensors 3 and 4 are on the bottom surfaces of the reactive specimens. Sensors 5 to 7 are on the back surfaces of the reactive specimens. Sensors 8 to 10 are on the front surfaces of the reactive specimens. Sensors 11 and 12 are on the back surface of the control specimen. Sensors 13 and 14 are on the front surface of the control specimen. The sensors were attached on the surface of the specimens using epoxy, and constant pressure was applied to the surface of the sensors through specially designed and fabricated holders (Soltangharaei et al. 2018). The sensor-to-cable connections were protected with heat shrink tubing.

A 24-channel Micro-II Express, manufactured by MISTRAS Group. (Princeton Junction, New Jersey), was utilized for data acquisition with a sampling rate of 5 million samples per second. Equipment settings are provided in Table 2.

Concrete mixture proportions are presented in Table 3. In the reactive specimens, only the coarse aggregate was reactive. The reactive coarse aggregate was crushed greenschist from North Carolina. The nonreactive coarse aggregate (used in the control specimen) was crushed dolomite from Alabama. The nonreactive fine aggregate used in all specimens was dolomitic limestone sand from Alabama. The cement used in the mixture was an ASTM C150 Type I/II low-alkali cement with 0.48% Na_2O_{eq}. Sodium hydroxide (NaOH) was added to the two reactive specimens to increase the total alkali loading to 1.50% by mass of cement to accelerate the development of ASR.

The specimens were supported on specially designed and fabricated steel carriers with wheels. The contact surfaces of the

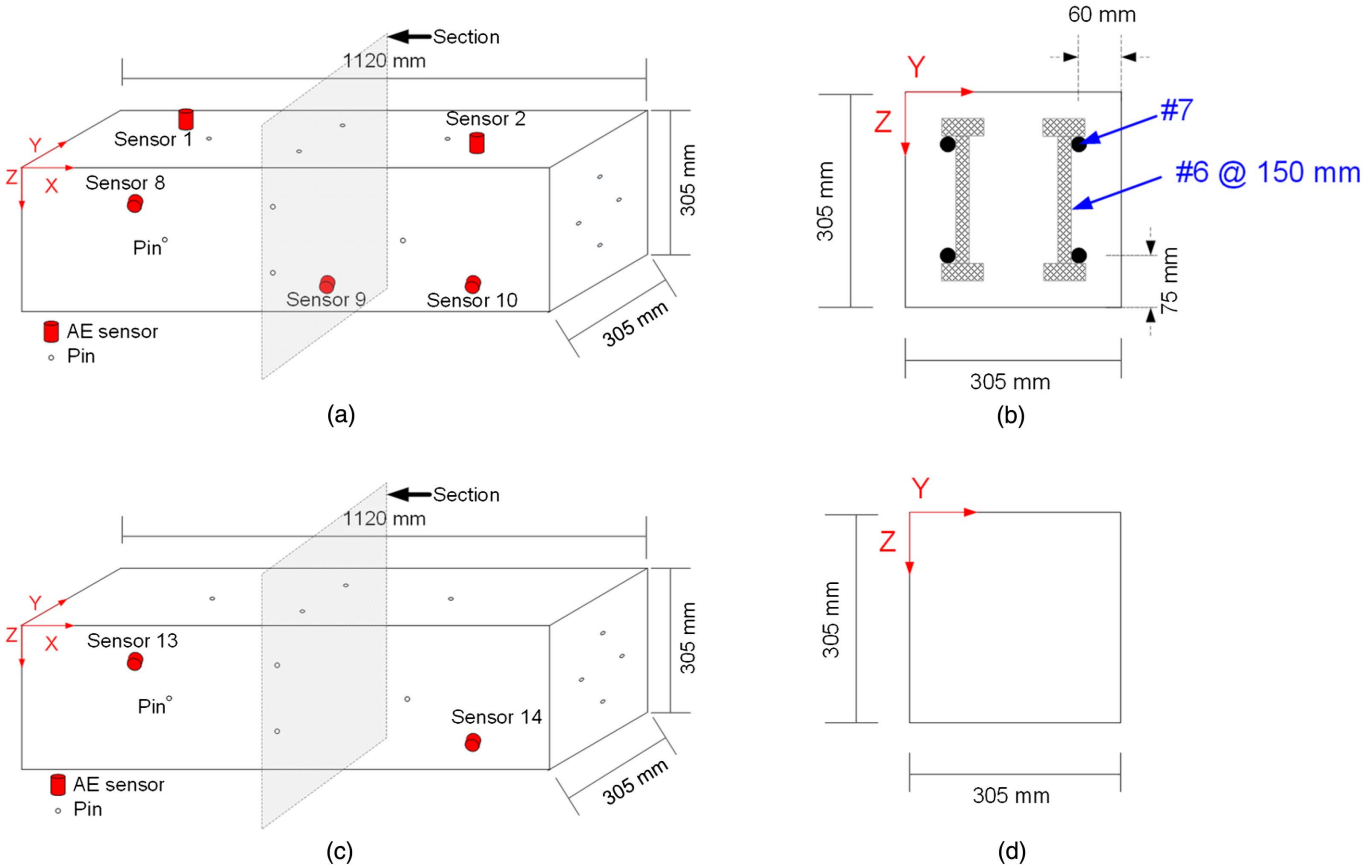

Fig. 1. Specimen sensor layouts and structural details: (a) confined and unconfined; (b) section for confined specimen; (c) control specimen; and (d) section for unconfined and control specimens.

Table 1. Sensor coordinates

Confined and unconfined specimens				Control specimen			
Sensor ID	X (mm)	Y (mm)	Z (mm)	Sensor ID	X (mm)	Y (mm)	Z (mm)
Sensor 1	279	229	0	Sensor 11	279	305	229
Sensor 2	838	76	0	Sensor 12	838	305	76
Sensor 3	279	76	305	Sensor 13	279	0	76
Sensor 4	838	229	305	Sensor 14	838	0	229
Sensor 5	279	305	229	—	—	—	—
Sensor 6	483	305	76	—	—	—	—
Sensor 7	838	305	76	—	—	—	—
Sensor 8	279	0	76	—	—	—	—
Sensor 9	635	0	229	—	—	—	—
Sensor 10	838	0	229	—	—	—	—

Table 2. Data acquisition setting

Sampling rate	Threshold	Pretrigger time	Hit definition time	Peak definition time	Hit lockout time	Low-pass digital filter	High-pass digital filter
5,000 kHz	32 dB	256 μs	400 μs	200 μs	200 μs	400 kHz	20 kHz

carriers were covered by neoprene pads to minimize the transference of potential vibrations and noise from the ground.

The specimens were retained inside a chamber with dimensions of 243 cm(width) × 243 cm(length) × 122 cm(height). The temperature and humidity of the chambers were kept at 37 ± 3°C and 95% ± 5% during the test with the exception of scheduled shutdown dates (for expansion measurement and maintenance).

Pins were attached to the specimens using gray double/bubble epoxy with the extra fast setting for DEMEC gauge measurement (demountable mechanical strain gauges). The schematic locations of the pins are illustrated in Fig. 1 (black empty ellipse). Four pins were located on each surface of the specimens except for the bottom surface with the arrangement shown in Fig. 1. It should be noted that the pin arrangements for the left and back surfaces of the

Table 3. Concrete mixture proportions

Mixture components	Quantity (kg/m^3)	
	Control specimen	Reactive specimens
Cement	350	350
w/c ratio	0.5	0.5
Nonreactive coarse aggregate	1,140	—
Reactive coarse aggregate	—	1,050
Nonreactive sand	752	851
NaOH solution (50% w/w)	—	9.22

specimens were identical to the arrangements on the right and front surfaces. The distance between the pins, parallel to the X axis, was 500 mm, and the distances between the pins parallel to the Y and Z directions were 150 mm. The epoxy had a high durability and humidity resistance and was suitable to bond to concrete. The displacement measurements between the pins were conducted monthly on each surface of the specimens using DEMEC gauges with gauge lengths of 500 mm for the X-direction (length) measurements and 150 mm for Y- and Z-direction (height and width) measurements, respectively. The expansion strains were calculated by dividing the displacement differences between each measurement and initial measurement by the gauge lengths. The DEMEC gauge measurements were started at 48 days after casting the specimens. Measurement of the crack width was begun at 146 days after casting using a Dino-Lite digital microscope with a maximum magnification of 184 X (Leica Microsystems, Buffalo Grove, Illinois) and a crack detection microscope with a magnification of 40 X (EIE International, Leighton Buzzard, UK).

Analysis Procedure

The AE data were continuously collected for 300 days, with the exception of maintenance and expansion measurement time periods. Filters were developed to minimize nongenuine AE data. After filtering, an unsupervised pattern recognition algorithm was employed to aid in classification of the remaining data. The data were localized using an iterative algorithm and modified times of arrival (TOA) of the classified events. Contour graphs were developed to show the potential damage locations.

A filtering procedure based on AE event definition has been utilized to remove the potential nongenuine data. AE data that were registered by at least four sensors within a specific wave travel time were retained, and AE data that were registered by three or fewer sensors were removed. The wave travel time is a maximum time that a stress wave travels from a source to a sensor in the specimen. In other words, the AE events that had at least four hits were kept, and the rest of the data were deleted. The waveforms of data after filtering were visually further checked, and the potential remaining nongenuine data were deleted.

Unsupervised Pattern Recognition Algorithm

In this section, a detailed explanation for the unsupervised pattern recognition algorithm utilized in this paper is provided (Fig. 2). The AE signals were initially transferred to the frequency domain by using fast Fourier transform (FFT). The frequency domain of each signal was divided by 10 equal portions with bandwidths of 40 kHz. The energies corresponding to each frequency band were derived by

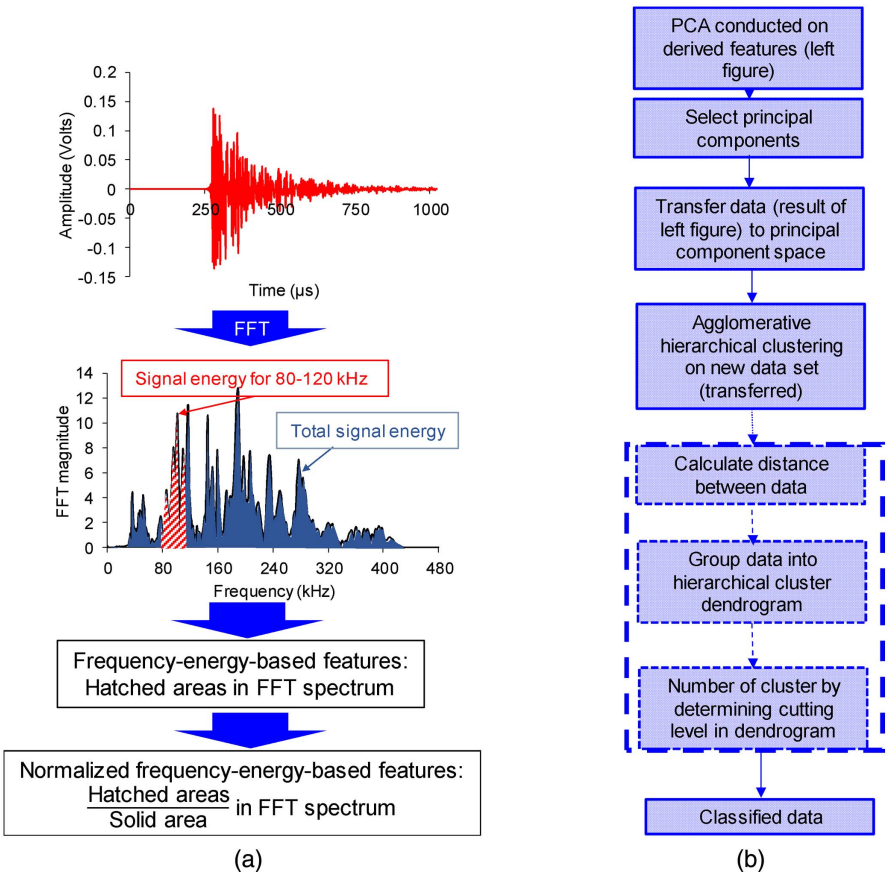

Fig. 2. Unsupervised pattern recognition procedure: (a) frequency-energy feature extraction; and (b) principal component feature extractions and clustering steps.

J. Mater. Civ. Eng., 2020, 32(10): 04020285

calculating the area under the FFT spectrum in that frequency band [e.g., hatched area in Fig. 2(a)]. The energies in the frequency bands were normalized to the total energy of the signal, which was calculated by the area under FFT spectrum [shown as a solid area in Fig. 2(a)]. These normalized energies for different frequency bands are referred to as frequency-energy–based features in this paper (Soltangharaei et al. 2018). Principal component analysis (PCA) was conducted on the extracted frequency-energy–based features to reduce feature redundancy [Fig. 2(b)]. Eigenvalues and eigenvectors of a covariance matrix of frequency-energy–based features were calculated in PCA. Eigenvectors represented the principal components (PCs) or the direction of new coordinates. The PCs, which had the largest eigenvalues, were selected to reduce the redundancy. The first four PCs, which contained more than 93% of the information of data distribution, were selected in this paper. The data, which contained frequency-energy–based features [resultant of procedure in Fig. 2(a)], were transferred to the new space defined by the selected PCs (Jolliffe 2002; Tan et al. 2018). These transferred data were used as an input for the agglomerative hierarchical algorithm [Fig. 2(b)]. The aglomorative hierarchical algorithm has three main steps, as shown in [Fig. 2(b)]: calculating distance between data, grouping data into the clusters, and determining the final cluster number. First, Euclidean distances between the new features (based on PCs) were calculated. The result was a matrix, which contained the distances between the data (dissimilarity matrix). Then, the data, which were close to each other, were paired in a binary cluster. Then, the paired data were also grouped and formed new clusters. This procedure continued to include all the data and resulted clusters. The final result was a cluster tree or a dendrogram, which included several upside-down U-shaped lines (links) (Bouguettaya et al. 2015). The heights of the U-shape links illustrate the distances between clusters and original data, and the horizontal axis indicates data labels. Original data is labeled through algorithm, and some labels are indicated on the horizontal axis. In this study, the data and resulted clusters were linked through a procedure referred to as Ward's method, as described in (Murtagh and Legendre 2014). The number of clusters (cutting level) was determined based on the dendrogram and the height of each link with respect to the average height of its following links. (Bouguettaya et al. 2015).

Source Localization and Modification of Time of Arrival

One method for source localization of AE data is the TOA approach (Ge 2003a, b). This method is based on the TOAs of signals registered in each sensor and solving a nonlinear equation of velocity versus distance. Estimating a realistic TOA for signals has a direct effect on the source location precision. Most commercial AE data visualization software has two options for estimating TOAs (i.e., peak timing and first time crossing), which are based on peak time and threshold (Mistras-Group 2014). These methods often do not result in realistic TOAs, especially when the source is far away from the sensors due to wave dispersion and attenuation. The errors related to TOAs increase in heterogeneous materials such as concrete in comparison to homogeneous materials. Therefore, in this study, the Akaike Information Criterion (AIC) was utilized for estimating the TOAs. This method has shown relatively good results in previous research investigations for concrete (Carpinteri et al. 2012; Van Steen et al. 2019). In this method, a window is defined at the beginning of the signal to include the region of the expected signal initiation. In this study, the first 356 μs of each signal is considered for TOA calculation. For the windowed signals, the AICs are calculated according to the following equation (Akaike 1998; Carpinteri et al. 2012)

$$AIC(t_w) = t_w \log(\sigma^2(S(1{:}t_w))) + (n_w - k_w)\log(\sigma^2((1+t_w){:}n_w)) \quad (1)$$

where n_w = last point of the windowed signal (in this paper, equal to the sample point corresponding to 356 μs); S = signal voltage value for all samples; t_w = desired sample point for calculating the AIC, which ranges from 1 to n_w; and σ^2 = variance of signal voltages in the desired range. The AICs are calculated for all sample points in the windowed signals, and the minimum values denote TOAs of the signals.

Another factor that can affect the source location results is the selection of appropriate signals (hits) in an event. Each event may have more than four hits [the minimum hit number for three-dimensional (3D) source location], some of which are very weak, and it is hard to find the TOA even by using AIC. Therefore, a method (Carpinteri et al. 2012) based on the second derivative of AIC was employed for hit selection in an event. The certainty levels (CL) of calculated TOAs are calculated by the following equation (Carpinteri et al. 2012)

$$CL = [AIC(t_{\min} - \delta t) + AIC(t_{\min} + \delta t) - 2AIC(t_{\min})]/\delta t^2 \quad (2)$$

where $t_{\min}$ = time in a signal corresponding to the minimum AIC; and δt = small-time interval around the estimated TOA (minimum AIC). This parameter is set to 15 μs for the data in this study. The lower values for CL indicate unreliable estimated TOA by AIC and can be deleted if a sufficient number of hits exists. In this study, the five hits with the largest CL values in each event are only considered for the source localization.

After TOA estimation and selection of the appropriate signals, an iterative source localization algorithm was used to determine the source location. The minimum difference between the calculated and observed TOAs is considered as a source location solution. This procedure was conducted by using a nonlinear least-squares method algorithm (Ge 2003b; Torkjazi et al. 2018). The wave velocities in the algorithm were estimated based on Pencil Lead Break (PLB) tests, which were conducted during the test.

The results of source locations are presented in contour diagrams by considering the cumulative signal strength of the events. The specimens were initially meshed, with the enclosed area in each mesh referred to as a cell. Then, a customized code was developed to read the input file, which was the result of the source location, and weight values were assigned to the nodes in each cell according to the average signal strength of each event. The weight values for each cell were updated when a new event occurred inside the cell, with the average signal strength of the new event added to the previous cumulative signal strength in the cell. The weights in all cells were normalized to the maximum weight at the end of the test. The result is a contour diagram corresponding to the concentration of damage. The color in the contour corresponding with the largest value illustrates the location with the emission of events with the largest signal strength, and/or a large number of events occur in those locations.

Results and Discussion

The strains measured on the surfaces in each direction (e.g., X, Y, and Z directions) were averaged and denoted as average strain [Fig. 3(b)]. The volumetric strain is defined as the accumulation of average strains along the axes of X, Y, and Z. Results of volumetric strain and average strains in the X, Y, and Z directions are presented in Fig. 3. For example, the average strain for the confined specimen along the X axis is indicated by the label Confined X in Fig. 3, and is the average of strains along the X axis on the front,

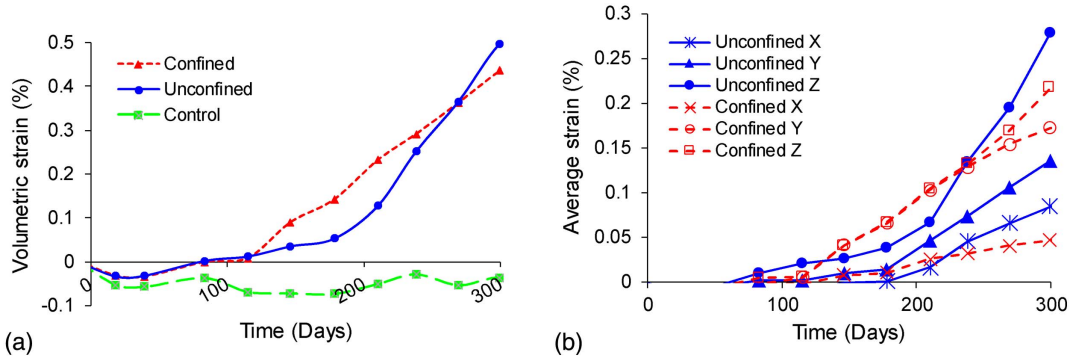

Fig. 3. Measured strains using DEMEC gauge: (a) volumetric strain; and (b) average strain.

back, and top surfaces of the confined specimen. The reactive specimens expanded; the control specimen did not. The volumetric strain for the confined specimen increased with a higher rate than the unconfined specimen at around 115 days, whereas the volumetric strain for the unconfined specimen reached the value for the confined specimen at 269 days. Based on the measured volumetric strain, comparatively more severe cracking is expected for the confined specimen than the unconfined specimen between 115 and 220 days. The larger volumetric strain of the confined specimen compared to the unconfined specimen (115–269 days) was primarily due to the larger strains in the Y and Z directions. This might be due to anisotropic expansion and cracking due to the reinforcement. According to the numerical model proposed in (Morenon et al. 2017), the ASR gel pressure increased by loading and restraint. The ASR gel pressure caused cracks perpendicular to the loading or restraint directions.

In the confined specimen, the reinforcement might cause an increase in the ASR gel pressure and simultaneously limited the paths for reducing the pressure. This might cause the anisotropic expansion and the larger expansion rate in the confined specimen between 115–269 days.

Another possible reason for the larger volumetric strain of the confined specimen might be the different distribution of relative humidity in the specimens due to the heterogeneous concrete characteristics and reinforcements in the confined specimen.

Unconfined specimen: The average strain in the Z direction (specimen depth) exceeds that in the other two directions [Fig. 3(b)], potentially due to the lower tensile strength of the concrete along the direction perpendicular to casting (Smaoui et al. 2004). The decreased tensile strength may be associated with a thicker film of bleed water accumulating under aggregates, causing increased porosity and weaker interfacial transition zones around the aggregates. In addition, flat and elongated aggregate particles tend to be preferentially oriented along the plane parallel to the casting direction in concrete, and aggregates having larger specific surface area tend to produce more gel due to ASR (Smaoui et al. 2004).

Confined specimen: The strains in the Y and Z directions (width and depth) are almost the same until 238 days. The strains in the Y and Z directions are larger than those in the longitudinal (X) direction. The large strain in the Z direction, despite the confinement, may also be associated with the casting direction effect. It should be noted that the measurement points for Z-direction expansion were located between the vertical reinforcing bars where confinement may have been locally minimized and this may have contributed to the observed effect. In addition, the confinement along the Z direction caused a redistribution of the ASR-induced stress in the Y direction. This caused a lager expansion along the Y axis.

The confined/unconfined strain ratio in the Y direction approaches 2.25. Therefore, more cracks with a larger width oriented parallel to the X direction are expected in the confined specimen, particularly.

Both the number of hits and the cumulative signal strength (CSS) for the control specimen are much less than for the two reactive specimens. Larger amounts of AE activity are observed in the confined versus the unconfined specimen (Fig. 4). The blank gaps in the figure are mostly related to the shutdown times during the experiment due to the maintenance of the chamber, checking the controller system, checking the sensors, and expansion measurements. In addition, the rate of AE events in the unconfined specimen is much less than the rate for the confined specimen. In some intervals, especially for the unconfined specimen, no events with more than three hits were recorded by the system. Therefore, the data in the unconfined specimen appears less dense than the confined specimen.

Frequency-Based Observations

The data for the confined and unconfined specimens were classified into four clusters and three clusters, respectively. C1 to C4 are for the confined specimen, and U1 through U3 are for the unconfined specimen (Fig. 5). The number of clusters was determined based on the height of links in the dendrograms, and desired levels for clustering are indicated by the corresponding lines in the figure. A detailed explanation was provided in the section on the unsupervised pattern recognition algorithm. Fig. 5 shows the resulted dendrograms for confined and unconfined specimens. The horizontal axis in Fig. 5 shows data labels and the vertical axis indicates the distances between the data or clustered data. The vertical axis was calculated based on the normalized data. Therefore, the values of the vertical axis do not have any unit. Each label number on the horizontal axis presents one of input data. Some data labels were shown on the horizontal axis of Fig. 5 due to the large amount of data and limited length of horizontal axis. The data set, which had 10 frequency-energy features, were condensed by PCA and transferred to the PC space, as explained in the section on the unsupervised pattern recognition algorithm. Fig. 6 represents the transferred data in the PC space. Four PCs with the largest eigenvalues were selected for clustering, while the data were only able to be presented in terms of the first three PCs. Several data in each cluster are at cluster boundaries due to sharing similar frequency-energy–based features (Figs. 6 and 7).

The average energy distribution in the frequency domain is presented in Fig. 7. The vertical axis is normalized energy calculated for each signal based on the energies enclosed in the frequency bands and normalized to the total energy of the signal.

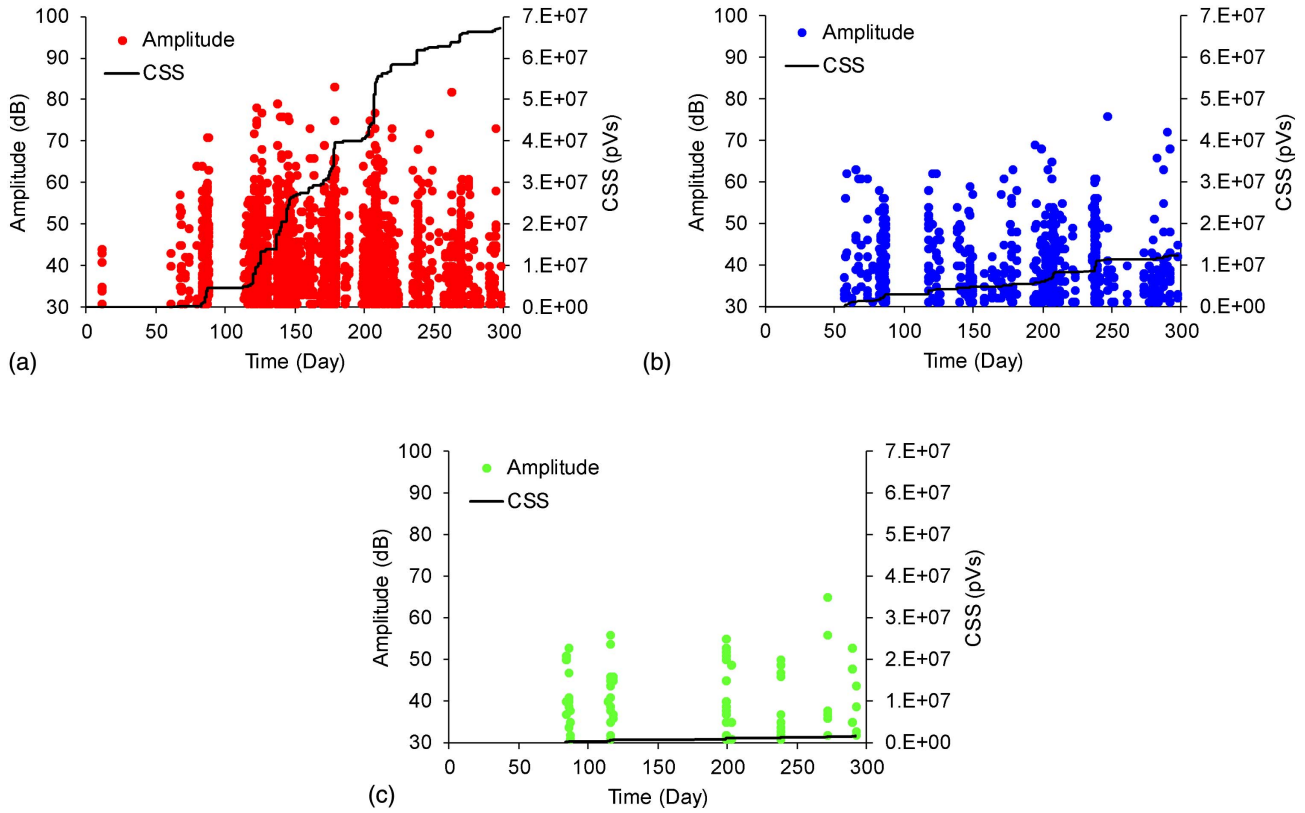

Fig. 4. Filtered AE data in terms of amplitude and cumulative signal strength versus time: (a) confined specimen; (b) unconfined specimen; and (c) control specimen.

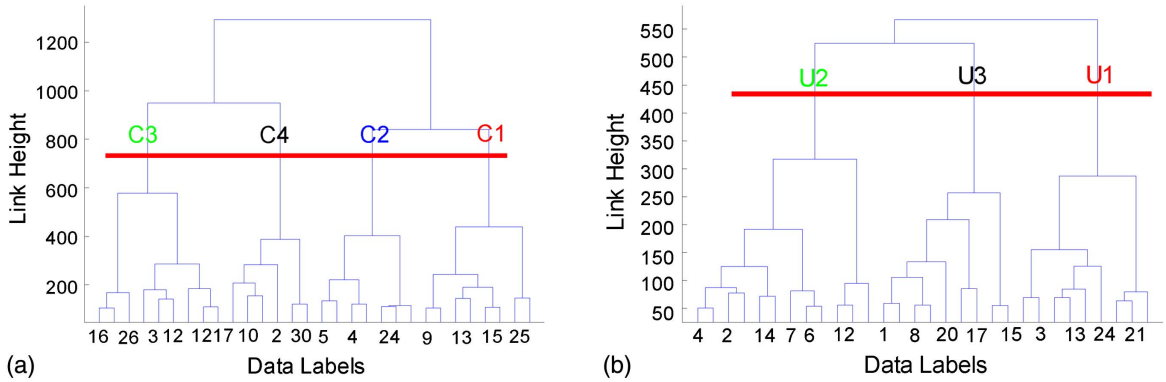

Fig. 5. Clustering dendrograms: (a) confined specimen; and (b) unconfined specimen.

Confined specimen: C1 and C2 are referred to as a low frequency. C3 has 45% energy in the frequency range of 80–120 kHz and is referred to as a medium frequency. C4, referred to as a high frequency, has the largest energy portion (63%) in frequencies of 80–200 kHz and distributed almost uniformly, and the highest distribution between 200–280 kHz among the clusters.

Unconfined specimen: U1 has 77% energy in the frequency range of 0–120 kHz and is referred to as a low frequency. U2 has the largest energy concentration (44%) in the range 80–120 kHz and is referred to as a medium frequency. U3 has 57% energy in the frequency range of 80–200 kHz and is referred to as a high frequency.

The CSS curves in terms of time for the clusters are shown in Fig. 8. The signal strengths of data in each cluster were added during the experiment time for each specimen. The CSS values for each cluster in a specimen were normalized to the maximum final CSS of all clusters attributed to that specimen (Fig. 8). Therefore, the CSS values in this figure are unitless.

Confined specimen: The CSS for the medium frequency (C3) increases abruptly at 115 days, coinciding with the sudden increase in strain rates in the Y and Z directions. The activity rate starts to decrease after 200 days when the expansion rate in the Y direction decreases.

Unconfined specimen: Strain rates in both the Y and Z directions increase modestly up to 178 days, as reflected in the AE data. Strain rate started to increase between 178 and 270 days, especially in the Z direction, causing an increased rate in AE data. The CSS increases significantly, especially in U2, and later in U1 between 180 and 250 days.

J. Mater. Civ. Eng., 2020, 32(10): 04020285

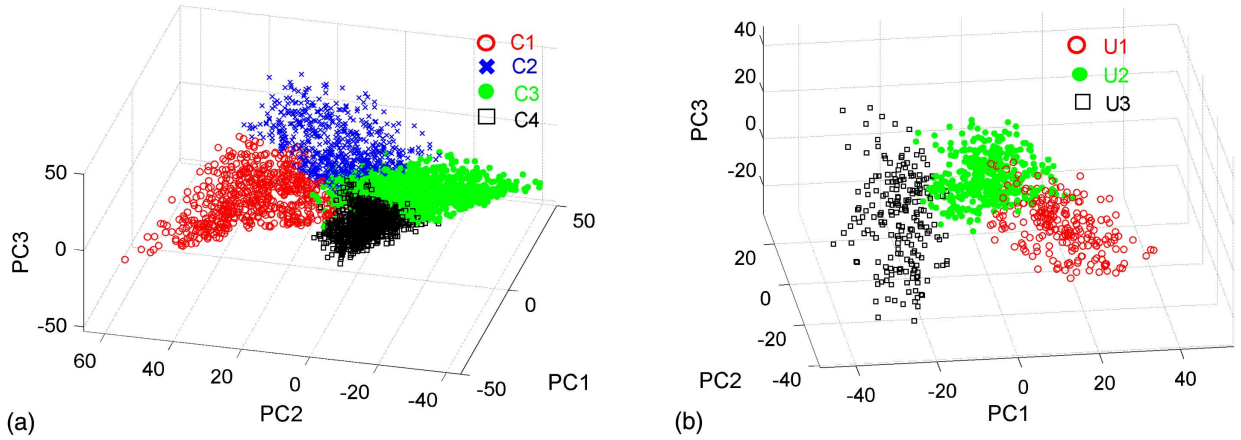

Fig. 6. Data presentation in principal component space: (a) confined specimen; and (b) unconfined specimen.

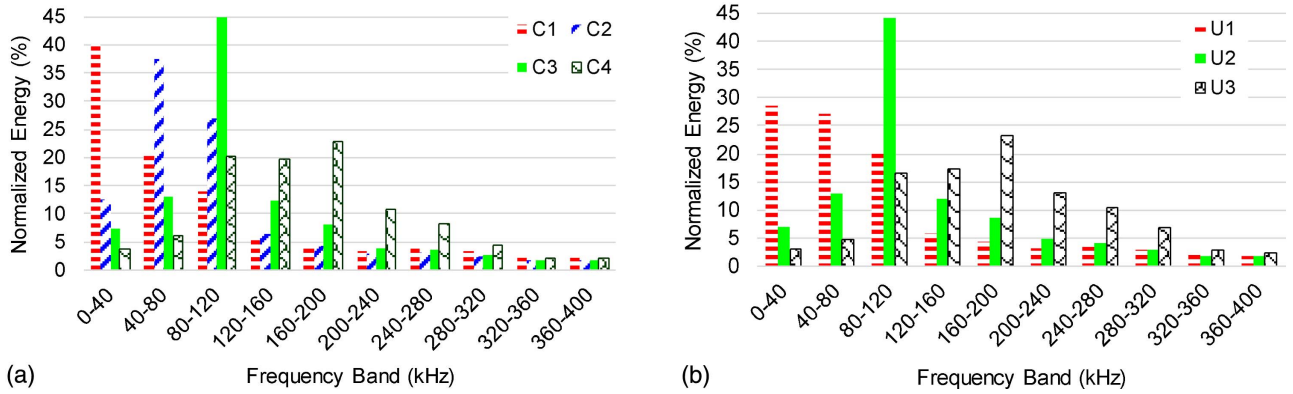

Fig. 7. Energy-frequency distributions of clusters: (a) confined specimen; and (b) unconfined specimen.

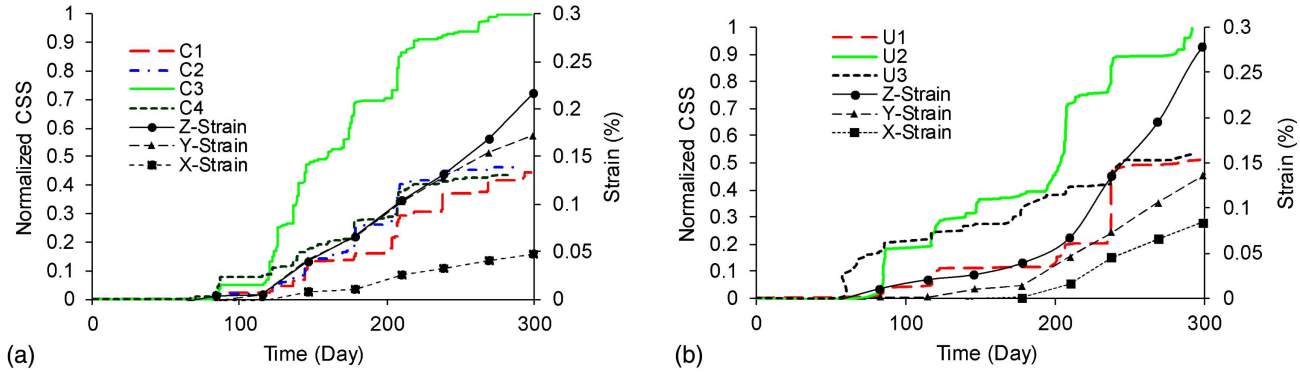

Fig. 8. Cumulative signal strength for clustered data: (a) confined specimen; and (b) unconfined specimen.

These observations indicate correlations between anisotropic expansion caused by ASR and CSS rates for clusters with differing frequencies. To investigate this further, the number of signals in each cluster within the specific time intervals was calculated and normalized to the total number of AE signals in those intervals (Fig. 9). In Fig. 9(a), the number of signals in C1 and C2 is compared with the number of signals in C3 and C4. In Fig. 9(b), the number of signals in U1 is compared with the number of signals in U2 and U3. The signals in C1 and C2 in the confined specimen have similar frequency contents as the signals in U1 in the unconfined specimen. The signals in C1, C2, and U1 have a large energy portion in the lower frequencies 0–120 kHz, while the signals in C3, C4, U2, and U3 have a large energy portion in the higher frequencies 120–240 kHz (referring to Fig. 7). The experiment duration has been divided into several intervals. In each interval, the percentage of low-frequency signals (C1, C2, and U1) was compared to the percentage of high-frequency and medium-frequency signals (C3, C4, U2, and U3).

In Fig. 9, for both confined and unconfined specimens, the percentage of low-frequency signals increased after 200 days.

J. Mater. Civ. Eng., 2020, 32(10): 04020285

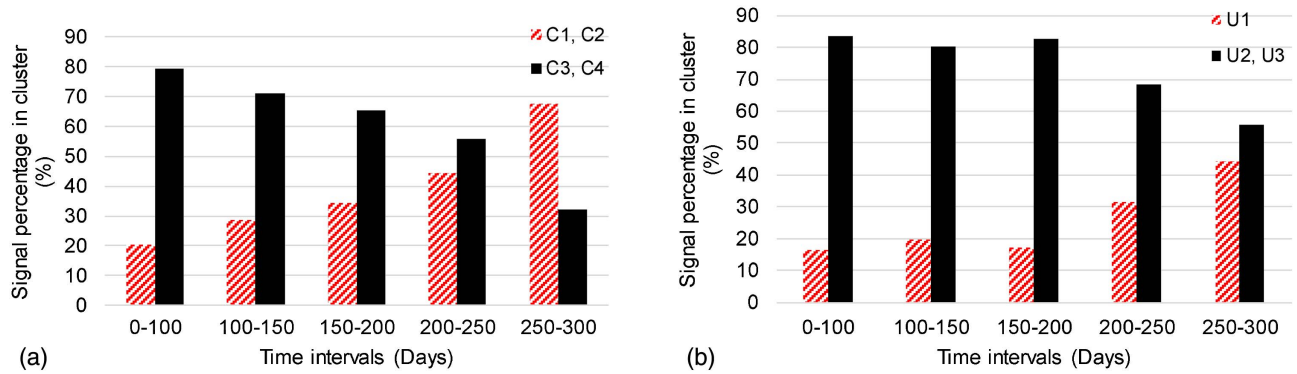

Fig. 9. Percentage of signals in clusters in terms of time: (a) confined specimen; and (b) unconfined specimen.

However, this increasing trend started earlier for the confined specimen than for the unconfined specimen. As the ASR process continued, more macrocracks were expected to form, and the existing cracks were expected to extend and merge. This was observed from visual surface macrocracks, which were increasing during the experiment especially at the later stage (after 200 days).

One possible explanation of the trends shown in Fig. 9 is that in the later stage of the ASR process, macrocrack formations and crack extension exceeded microcrack formation. In the literature, AE signals with low frequency have been attributed to crack extension, whereas AE signals with high frequency are attributed to the initiation of small-scale cracks (Lacidogna et al. 2017; Landis and Shah 1995). That may be the reason for observing a larger number of the low-frequency signals compared to the high-frequency signals. Another possible explanation is the wave scattering. In the later stages (after 200 days), the cracks become longer and wider, thereby increasing wave scattering, especially for higher-frequency signals. It was assumed that the defects caused discontinuities in the concrete and were located between the wave sources and the sensor locations. Moreover, the projection of the maximum defect size on the plane, perpendicular to the wave motion direction, was close to (or larger than) the wave lengths of high-frequency components of AE signals in the later stages (after 200 days). A third explanation may be provided (Farnam et al. 2015). In this study, Farnam et al. suggested that cracks due to ASR initiated inside the aggregates with the emission of high-frequency signals. As the ASR process continued, the cracks propagated inside the cement matrix with the emission of low-frequency signals (Farnam et al. 2015). However, this explanation depends on the aggregate type (Pan et al. 2012; Ponce and Batic 2006). In some aggregate types, cracks were observed inside aggregates in addition to the cement matrix. In other aggregates, cracks were mainly observed in the interfacial transition zones and the cement paste (Pan et al. 2012; Ponce and Batic 2006). In the specimens for the current investigation, cracks have been observed inside aggregates as well as in the cement matrix based on petrography results. Based on the AE data and visual observation, cracks are expected to generally initiate inside the aggregates and extend to the cement matrix.

The ASR gel may also form around or inside the aggregate depending on the aggregate type. The acoustic impedance of ASR gel is expected to be less than the cement matrix and aggregates, although the mechanical properties of the gel depend on the stress condition and Calcium concentration (Leemann and Lura 2013; Liu et al. 2015; Phair et al. 2005). Therefore, the gel may act as a barrier against the wave propagation and scatter the waves with high-frequency components.

The higher percentage of low-frequency signals in later stages of the ASR process may be explained by one of these hypotheses or a combination and is potentially the subject of future investigations.

Source Location and Event Distribution

Source localization was conducted for all events according to the procedure described in the section on source localization and modification of time of arrival, and contour diagrams were generated based on the source coordinates, source repetition in a cell, and cumulative signal strength in a cell. The diagrams for the unconfined and confined specimens in the X-Y plane are presented for 100, 200, and 300 days in Fig. 10. The contours show the spatial relative cumulative signal strength in each cell up to the desired times. The cumulative signal strength for each cell was normalized to the maximum CSS of cells at 300 days, and dimensions are shown in centimeters. The visual surface cracks apparent at 300 days are drawn on the contours to enable comparison. The continuous and dashed lines illustrate the surface cracks at the top and bottom of the specimens, respectively. The crack patterns in the confined and unconfined specimens are different. Most of the cracks in the confined specimens are parallel to the X direction, while the cracks in the unconfined specimen do not follow any specific pattern and are more randomly distributed in the X-Y plane along with both X and Y directions. The damage (cracking) in the confined specimen is more anisotropic than the unconfined specimen due to partial confinement applied by reinforcement in the X and Z directions. The confinement prevents free expansion in the X and Z directions and causes redistribution of ASR stress in the Y direction, consequently causing anisotropic cracking in that specimen.

Event distributions in the confined and unconfined specimens were generated along the Y direction. The examples of distributions are presented as histograms at 300 days in Fig. 11. The value in each bin was normalized to the total number of hits. Therefore, the sum of the bar heights in a specific distance range shows the relative probability of occurrence of the AE signals (distribution of AE events) and the total sum of the bar heights is equal to unity. The AE events in the confined specimen are more concentrated in the middle width of the specimen than the unconfined specimen. The continuous vertical lines in the distributions illustrate the median of the event distribution along the Y direction, and the dashed vertical lines show first and third quartiles of the event distribution along the Y direction. The first and third quartiles separate the lowest 25% of the data from the highest 75%, and the highest 25% of data from the lowest 75%, respectively.

To evaluate and quantify the concentration and distribution of the AE events along the Y direction, two parameters are calculated

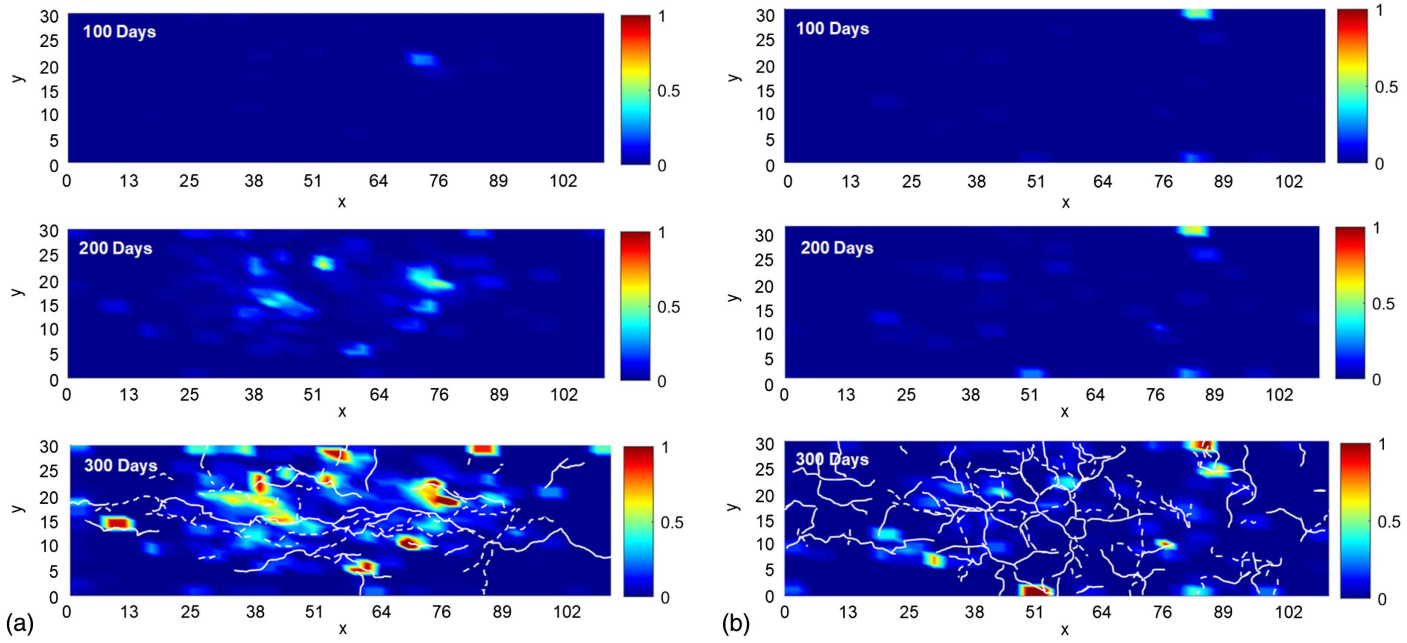

Fig. 10. Source localization contours in the X-Y plane (top view): (a) confined specimen; and (b) unconfined specimen.

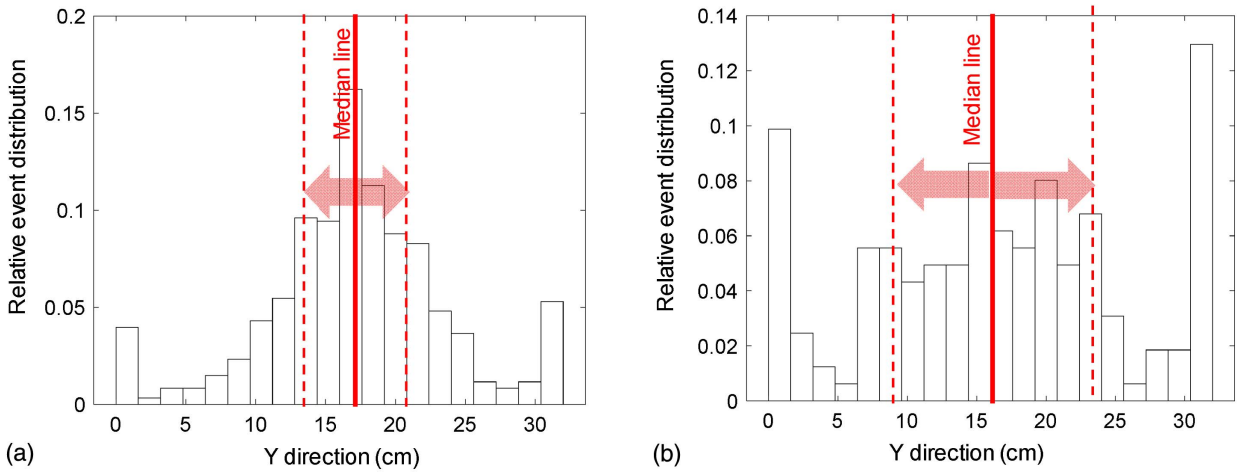

Fig. 11. AE event distributions in Y direction at 300 days: (a) confined specimen; and (b) unconfined specimen.

in terms of the experiment time. The first is calculated by summing the bar heights attributed to the middle 50% portion of specimen widths (8–24 cm). This value shows the relative probability of occurrence of AE events at the midwidth of the specimens [referred to as middle relative probability (MRP) in this paper]. In other words, MRP shows the ratio of the located events in the midsection of dimension (midwidth and midheight refer to the region between 8 and 24 cm of the associated dimensions).

The second parameter is the normalized interquartile range (IQR). This parameter is calculated by dividing the difference between the first and third quartiles by the specimen dimension. This parameter shows the concentration of event distribution in the midsection of dimension. For instance, MRP values for the confined and unconfined specimens for 300 days along the Y direction are 81% and 58%, respectively. This means that 81% of all events for the confined specimen are located between 8 and 24 cm. Furthermore, IQR values for the confined and unconfined specimens for 300 days along the Y direction are 22% and 43%, respectively, meaning that the distribution of the located AE events for the confined specimen is more concentrated than for the unconfined. The larger amount and concentration of AE events for the confined specimen in the midwidth of the specimen illustrates the consistency of the AE data with the expansion observations, and the anisotropic damage caused by the confinement imposed by the reinforcing steel is likewise observed in the AE data.

To further evaluate the behavior of the specimens due to ASR, the aforementioned parameters were calculated in terms of the experiment time and are presented graphically in Fig. 12. MRP values for the confined specimen are larger than the values for the unconfined specimen. In addition, IQR values for the confined specimen are much less than the IQR values for the unconfined specimen. This shows that the concentration of stress in the midwidth of the confined specimen is much larger than the unconfined specimen. The stress concentration causes the accumulation of AE events

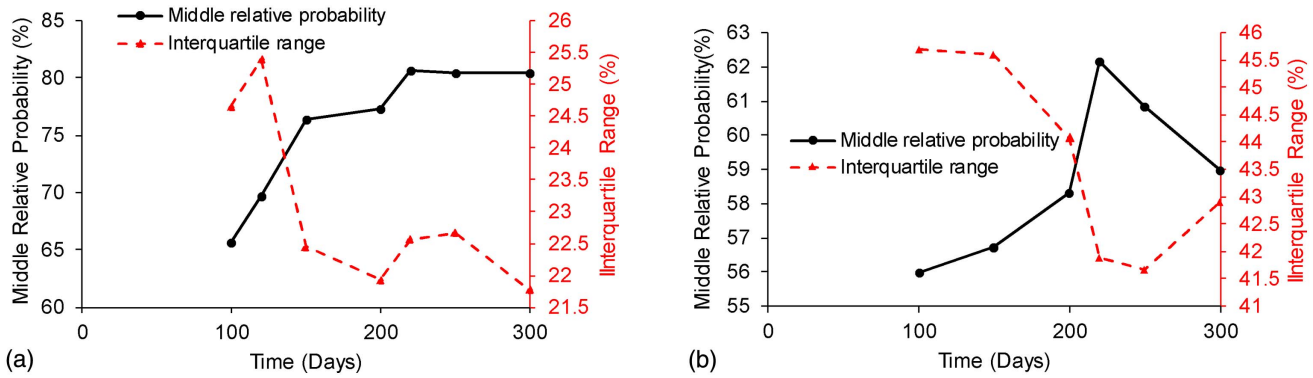

Fig. 12. AE event distribution parameters along Y axis versus experiment time: (a) confined specimen; and (b) unconfined specimen.

in the middle region of the confined specimen with the concentration of events around the median. In the unconfined specimen, the amount of AE events in the middle region increases up to 220 days and decreases thereafter. The increase rate is sharper between 200 and 220 days, which coincides with a major jump in the cumulative signal strength [Fig. 8(b)]. The AE events that occurred between 200 and 220 days were mainly concentrated in the middle region of the Y direction. The IQR values decreased as the MRP values increase, and vice versa.

Comparing Figs. 12(a and b), it can be concluded that in the confined specimen, damage concentration in the midwidth of the specimen (Y direction) starts earlier than in the unconfined specimen. The concentration of AE events for the confined specimen is much denser along the Y-axis from an earlier time (100 days) than for the unconfined specimen. On the other hand, the AE events are distributed (damage) more uniformly at 100 days along the Y direction in the unconfined specimen.

Source location contours for the X-Z plane are presented in Fig. 13. The continuous line shows the surface crack in the X-Z plane in the front view, according to Fig. 1 (Y = 0). The dashed lines show the surface crack in the backside of the specimen (Y = 31 cm). In the figure, Z = 0 is the top surface of the specimen. Cracks oriented in the longitudinal dimension (X direction) are observed in both confined and unconfined specimens (Fig. 13). These longitudinal cracks were caused due to anisotropic expansion. However, cracks also appeared along with the height of the unconfined specimen (Z direction). In the confined specimen, fewer cracks are oriented in the Z-direction (specimen height) than the unconfined specimen. This may be due to the longitudinal confinement provided by the steel reinforcement in the confined specimen along the X direction.

Distributions of the AE events located along the Z direction (specimen height) were also evaluated. An example of event distribution along the Z direction at 300 days is illustrated in Fig. 14. The MRP values were calculated by summing the bar heights attributed to the middle 50% portion of specimen heights (8–24 cm). The MRP values at 300 days for the confined and unconfined specimens are 71% and 50%, and IQR values are 30% and 50%, respectively. This shows a larger concentration of the AE events at the midheight of the confined specimen than the unconfined specimen. As mentioned, the casting direction may cause anisotropic expansion due to ASR in the specimen height. This expansion causes

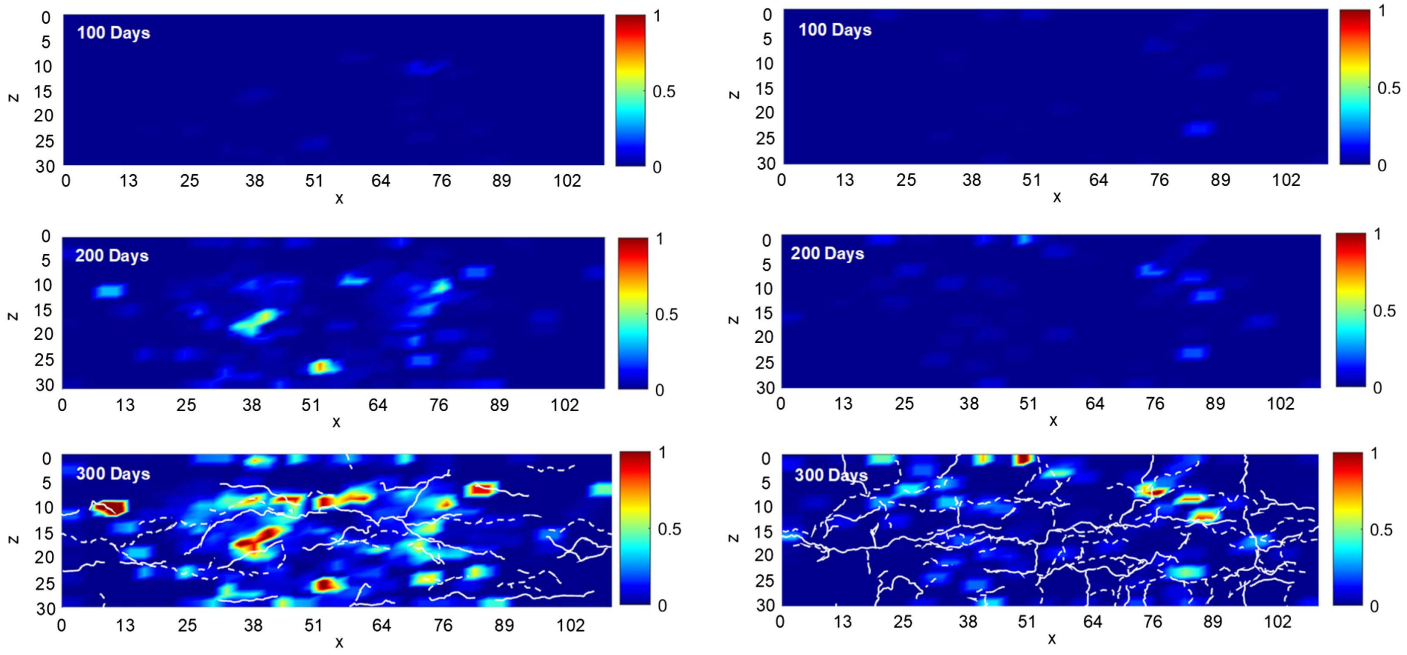

Fig. 13. Source location contours in X-Z plane.

J. Mater. Civ. Eng., 2020, 32(10): 04020285

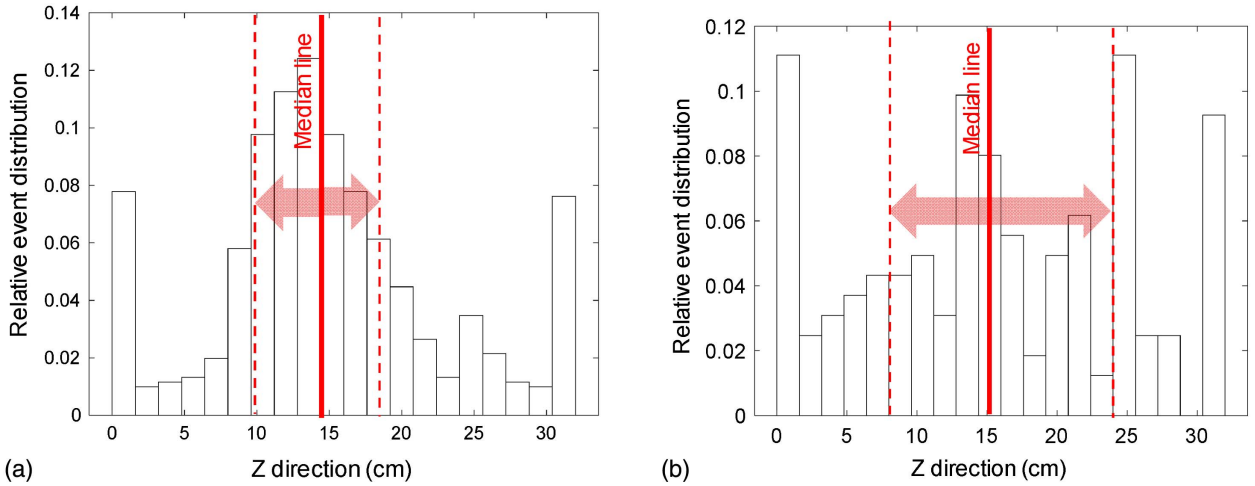

Fig. 14. AE event distributions in the Z direction at 300 days: (a) confined specimen; and (b) unconfined specimen.

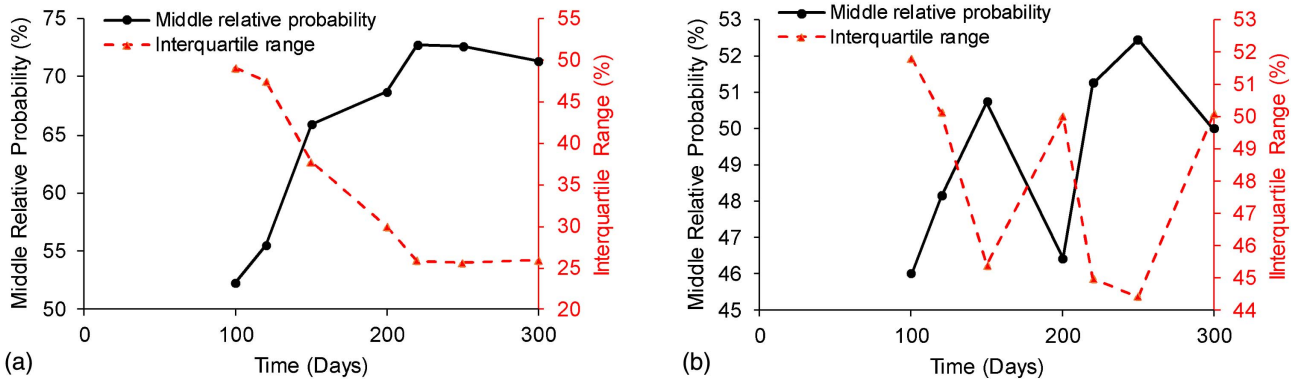

Fig. 15. AE event distribution parameters along Z axis versus experiment time: (a) confined specimen; and (b) unconfined specimen.

stress concentration in the confined specimen in the Z direction. The transverse reinforcements may affect stress distribution in the Z direction. The variation of the MRP and IQR in terms of time for the confined and unconfined specimens is presented in Fig. 15. In the confined specimen, the MRP increases at a larger rate up to 150 days, and the increasing rate diminishes thereafter. The events in the unconfined specimen do not show any trend of absolute increase or decrease, and the MRP values of the event fluctuate in terms of time. This shows that damage distributed more randomly along the height of the unconfined specimen compared to the confined specimen.

The MRP values for the confined specimen along the Z direction at 300 days are smaller than the corresponding value along the Y direction, which supports observations about anisotropy caused by the confinement along the specimen width.

Surface Crack Measurements

As mentioned in section on test setup and procedure, crack widths were measured beginning at 146 days after casting. The focus of this measurement was the visual cracks on the top surfaces of specimens. Examples of crack measurements are shown in Fig. 16. The figure depicts the cracks with the largest width at 269 and 300 days. The maximum crack widths were not necessarily attributed to the same crack and same location during the ASR process. Figs. 16(a and c) are related to a crack on the confined specimen, which was oriented in the X direction (parallel to the confinement plane). Figs. 16(b and d) are related to the cracks on the unconfined specimen, which were oriented in both the X and Y directions. The magnification in the pictures is 184X. The widths of cracks for the top surface of the confined and unconfined specimens in terms of time are illustrated in Fig. 17. As seen in the figures, the maximum crack widths on the top surface of the confined specimen are larger than those on the unconfined specimen. Furthermore, there are more visible cracks observed on the top surface of the confined specimen than on the unconfined specimen at 146 days.

The wider crack widths found on the confined specimen illustrate a larger stress concentration in the midwidth of the specimen when compared to the unconfined specimen, which is expected as the reinforcement in the confined specimen caused more anisotropic resistance to the ASR expansion. The midwidth of the confined specimen was more expanded than the unconfined specimen, and stress more concentrated in the midwidth of the specimen, which had the least restraint. Consequently, this led to wider cracks on the surface of the confined specimen. In addition, the stress concentration due to reinforcement in the confined specimen caused a larger number of cracks in the specimen at 146 days. The wider cracks and larger number of cracks earlier in the ASR process in the confined specimen are consistent with the AE results.

Petrographic Analysis

Petrographic analysis was conducted on the reactive specimens at the end of the accelerated aging process, and a summary of results

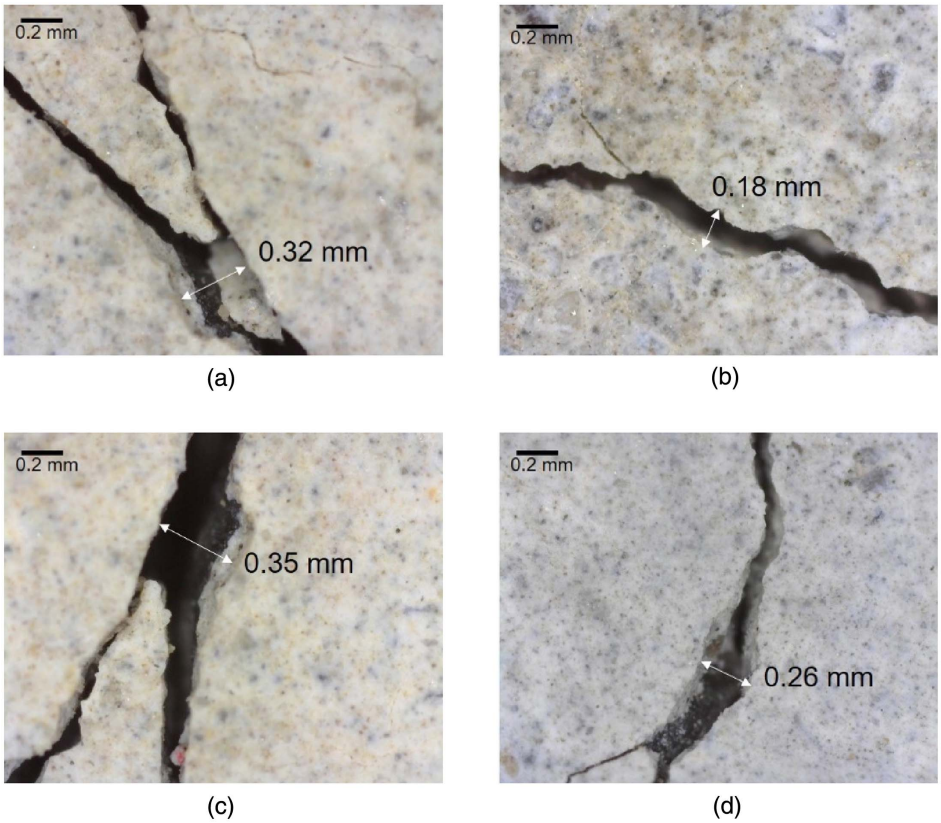

Fig. 16. Maximum crack width measurement: (a) confined specimen at 269 days; (b) unconfined specimen at 269 days; (c) confined specimen at 300 days; and (d) unconfined specimen at 300 days.

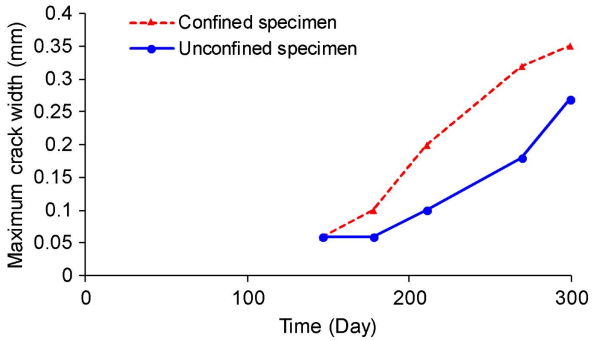

Fig. 17. Crack quantification on top surface in terms of time.

is provided in this section. The primary results indicated the presence of fresh ASR gel and calcium-rich ASR product in both reactive specimens in cracks, around coarse aggregates, and voids. Although the authors plan a future article detailing the correlation of internal damage, mechanical properties, and acoustic emissions, a brief summary of the petrographic investigation is provided below.

Cross-section slices were sawn from approximately one-half of the length of each specimen (core samples were extracted from the opposite half to measure mechanical properties). A total of 14 38-mm-thick cross-section slices were sawn from each specimen, with the cross-sections oriented parallel to the Y-Z plane. Each slice was further cut into quarter-sections and polished for stereo-optical microscopy examinations and a manual point count procedure (MPCP).

The MPCP was developed to provide a quantitative evaluation of internal damage in each beam. Although the DRI procedure can provide a more detailed quantitative description of damage from ASR in concrete, an alternate approach was needed to examine the full surface area of the cut sections. A 25 × 25-mm grid of 0.1-mm-thick lines was overlaid on each quarter-section. Each intersection point of the grid was examined at 20x magnification to characterize and quantify cracks present at that location (Fig. 18). Fine cracks refer to cracks less than 1 mm wide but visible without magnification, while microcracks refer to cracks that were only visible with magnification in the petrographic analysis. No coarse cracks with widths greater than 1 mm were observed in the grid intersections. Only cracks passing through the intersection were considered in MPCP.

Point count results were totaled for each slice including the four quarter-sections. The point count totals were multiplied by the weighting factors that assigned greater weight to cracks in the paste than cracks in the aggregate, with no distinction made between gel-filled and open cracks, a decision that was influenced by the DRI method recommended in Villeneuve et al. (2012). In this study, fine cracks also were weighted more than microcracks, because larger crack widths are assumed to correlate to a greater release of acoustic emission energy. The results for each slice were divided by the total number of points analyzed for that slice and multiplied by 100, which yielded the weighted normalized cracking score for the slice.

The MPCP was conducted on 13 full slices and one-half slice for the confined specimen and eleven slices for the unconfined specimen. The average results of slices for the confined and unconfined specimen are shown in Fig. 19 as weighted normalized cracking score. Generally, the cracking score for the confined specimen was larger than the unconfined specimen, which confirmed the

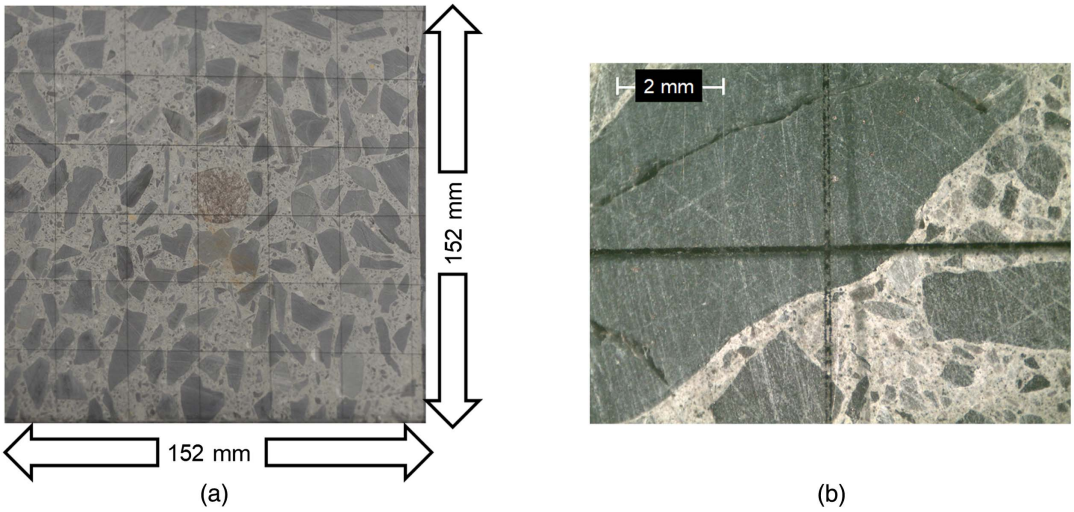

Fig. 18. Section preparation for petrographic analysis: (a) quarter section with grid; and (b) example of magnified grid intersection.

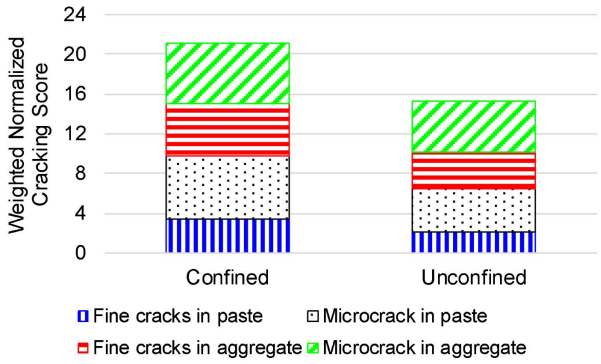

Fig. 19. Average of weighted normalized cracking score for reactive specimens.

results of surface cracking, expansion strains, and AE. It should be noted that the orientation of slices was perpendicular to the longitudinal reinforcement, which provided significant confinement against expansion in the X direction and led to anisotropic damage with expansions focused in the Y-Z plane. The cracking scores for the two show that the anisotropy of expansions and surface cracking are accompanied by similar differences in internal damage features.

Conclusion

The effect of confinement provided by longitudinal and transverse reinforcement was studied through data-driven methods. Unsupervised pattern recognition in combination with source location and statistical analysis were utilized. Three specimens were cast and exposed to high temperature and humidity for almost 300 days. Two specimens contained a reactive coarse aggregate, and the control specimen contained only nonreactive aggregates. One of the reactive specimens had confinement, provided through steel reinforcement, along with X and Z coordinates. The other reactive specimen and the nonreactive control specimen did not have any steel reinforcement. The ASR expansion was regularly measured with a DEMEC gauge. In addition, the crack widths on the top surface of the specimens were measured. The main conclusions of the study are summarized as follows.

The effect of the steel reinforcement on ASR damage distribution is clearly reflected in the AE data. More AE activity was detected in the confined specimen than in the unconfined specimen, with AE events concentrated in the midwidth region of the confined specimen, and these events exhibited almost normal distribution. The distribution of AE events for the unconfined specimen across the specimen width was more uniform. These observations in AE data correlate with anisotropic expansion in the confined specimen.

Damage from ASR in the confined specimen initiated earlier and was manifested in higher severity than the damage in the unconfined specimen; this can be observed from the AE data, expansion strains, and visible crack formation. The cumulative signal strength rate for the confined specimen increased abruptly in the 115 days (early stage of ASR). This behavior was not observed for the unconfined specimen. The volumetric strains for the confined specimen were greater than for the unconfined specimen up to 260 days. This difference between the volumetric strains was mainly due to very large strains for the confined specimen in the Y direction. Furthermore, the number of cracks in the confined specimen were greater than the unconfined specimen at 146 days (start of the crack measurement), and maximum crack widths on the top surface of the confined specimen was larger than the crack widths of the unconfined specimen.

Data Availability Statement

Some or all data, models, or code generated or used during the study are proprietary or confidential in nature and may only be provided with restrictions. This data includes acoustic emission, Demec, and crack width measurements. Data can be made available upon request and with the written permission of the sponsor.

Acknowledgments

This research was partially supported by the US Department of Energy-Nuclear Energy University Program (NEUP) under the contract DE-NE0008544 and the US Department of Energy Office of Science, Office of Basic Energy Sciences and Office of Biological and Environmental Research under Award Number DE-SC-00012530. The authors would like to acknowledge the contributions of the following RJ Lee Group petrographers and scientists: Patricia Kyslinger, Michael Baker, Blake Restelli, and April Snyder.

References

Abdelrahman, M., M. K. ElBatanouny, P. Ziehl, J. Fasl, C. J. Larosche, and J. Fraczek. 2015. "Classification of alkali–silica reaction damage using acoustic emission: A proof-of-concept study." *Constr. Build. Mater.* 95 (Oct): 406–413. https://doi.org/10.1016/j.conbuildmat.2015.07.093.

Akaike, H. 1998. "Information theory and an extension of the maximum likelihood principle." In *Selected papers of hirotugu akaike*, 199–213. New York: Springer.

Allard, A., S. Bilodeau, F. Pissot, B. Fournier, J. Bastien, and B. Bissonnette. 2018. "Expansive behavior of thick concrete slabs affected by alkali-silica reaction (ASR)." *Constr. Build. Mater.* 171 (May): 421–436. https://doi.org/10.1016/j.conbuildmat.2018.03.159.

ASTM. 2020. *Standard test method for determination of length change of concrete due to alkali-silica reaction*. ASTM C1293. West Conshohocken, PA: ASTM.

Barbosa, R. A., S. G. Hansen, K. K. Hansen, L. C. Hoang, and B. Grelk. 2018. "Influence of alkali-silica reaction and crack orientation on the uniaxial compressive strength of concrete cores from slab bridges." *Constr. Build. Mater.* 176 (Jul): 440–451. https://doi.org/10.1016/j.conbuildmat.2018.03.096.

Blanco, A., F. Pardo-Bosch, S. Cavalaro, and A. Aguado. 2019. "Lessons learned about the diagnosis of pathologies in concrete dams: 30 years of research and practice." *Constr. Build. Mater.* 197 (Feb): 356–368. https://doi.org/10.1016/j.conbuildmat.2018.11.143.

Bouguettaya, A., Q. Yu, X. Liu, X. Zhou, and A. Song. 2015. "Efficient agglomerative hierarchical clustering." *Expert Syst. Appl.* 42 (5): 2785–2797. https://doi.org/10.1016/j.eswa.2014.09.054.

Campos, A., C. M. Lopez, A. Blanco, and A. Aguado. 2018. "Effects of an internal sulfate attack and an alkali-aggregate reaction in a concrete dam." *Constr. Build. Mater.* 166 (Mar): 668–683. https://doi.org/10.1016/j.conbuildmat.2018.01.180.

Carpinteri, A., J. Xu, G. Lacidogna, and A. Manuello. 2012. "Reliable onset time determination and source location of acoustic emissions in concrete structures." *Cem. Concr. Compos.* 34 (4): 529–537. https://doi.org/10.1016/j.cemconcomp.2011.11.013.

Farnam, Y., M. R. Geiker, D. Bentz, and J. Weiss. 2015. "Acoustic emission waveform characterization of crack origin and mode in fractured and ASR damaged concrete." *Cem. Concr. Compos.* 60 (Jul): 135–145. https://doi.org/10.1016/j.cemconcomp.2015.04.008.

Garcia-Diaz, E., J. Riche, D. Bulteel, and C. Vernet. 2006. "Mechanism of damage for the alkali–silica reaction." *Cem. Concr. Res.* 36 (2): 395–400. https://doi.org/10.1016/j.cemconres.2005.06.003.

Ge, M. 2003a. "Analysis of source location algorithms Part 1: Overview and non-iterative methods." *Acoust. Emission* 21: 14–24.

Ge, M. 2003b. "Analysis of source location algorithms: Part 2. Iterative methods." *J. Acoust. Emission* 21 (1): 29–51.

Giannini, E. R., K. J. Folliard, J. Zhu, O. Bayrak, K. Kreitman, Z. Webb, and B. Hanson. 2013. "Non-destructive evaluation of in-service concrete structures affected by Alkali-Silica reaction (ASR) or delayed ettringite formation (DEF)—Final Report, Part I." Accessed May 24, 2020. https://library.ctr.utexas.edu/ctr-publications/0-6491-1.pdf.

Gorga, R., L. Sanchez, and B. Martín-Pérez. 2018. "FE approach to perform the condition assessment of a concrete overpass damaged by ASR after 50 years in service." *Eng. Struct.* 177 (Dec): 133–146. https://doi.org/10.1016/j.engstruct.2018.09.043.

Hariri-Ardebili, M. A., and V. E. Saouma. 2018. "Sensitivity and uncertainty analysis of AAR affected reinforced concrete shear walls." *Eng. Struct.* 172 (Oct): 334–345. https://doi.org/10.1016/j.engstruct.2018.05.115.

Hayes, N. W., Q. Gui, A. Abd-Elssamd, Y. Le Pape, A. B. Giorla, S. Le Pape, E. R. Giannini, and Z. J. Ma. 2018. "Monitoring alkali-silica reaction significance in nuclear concrete structural members." *J. Adv. Concr. Technol.* 16 (4): 179–190. https://doi.org/10.3151/jact.16.179.

Islam, M. S., and N. Ghafoori. 2018. "A new approach to evaluate alkali-silica reactivity using loss in concrete stiffness." *Constr. Build. Mater.* 167 (Apr): 578–586. https://doi.org/10.1016/j.conbuildmat.2018.02.047.

Jolliffe, I. T. 2002. *Principal component analysis*. New York: Springer.

Karthik, M. M., J. B. Mander, and S. Hurlebaus. 2016. "Deterioration data of a large-scale reinforced concrete specimen with severe ASR/DEF deterioration." *Constr. Build. Mater.* 124 (Oct): 20–30. https://doi.org/10.1016/j.conbuildmat.2016.07.072.

Kim, G., S. Park, J.-Y. Kim, K. E. Kurtis, N. W. Hayes, and L. J. Jacobs. 2018. "Nonlinear Rayleigh surface waves to characterize microscale damage due to alkali-silica reaction (ASR) in full-scale, nuclear concrete specimens." *Constr. Build. Mater.* 186 (Oct): 1114–1118. https://doi.org/10.1016/j.conbuildmat.2018.08.022.

Lacidogna, G., G. Piana, and A. Carpinteri. 2017. "Acoustic emission and modal frequency variation in concrete specimens under four-point bending." *Appl. Sci.* 7 (4): 339. https://doi.org/10.3390/app7040339.

Lahdensivu, J., A. Köliö, and D. Husaini. 2018. "Alkali-silica reaction in Southern-Finland's bridges." *Case Stud. Constr. Mater.* 8 (Jun): 469–475. https://doi.org/10.1016/j.cscm.2018.03.006.

Landis, E. N., and S. P. Shah. 1995. "Frequency-dependent stress wave attenuation in cement-based materials." *J. Eng. Mech.* 121 (6): 737–743. https://doi.org/10.1061/(ASCE)0733-9399(1995)121:6(737).

Leemann, A., and P. Lura. 2013. "E-modulus of the alkali–silica-reaction product determined by micro-indentation." *Constr. Build. Mater.* 44 (Jul): 221–227. https://doi.org/10.1016/j.conbuildmat.2013.03.018.

Liaudat, J., I. Carol, C. M. López, and V. E. Saouma. 2018. "ASR expansions in concrete under triaxial confinement." *Cem. Concr. Compos.* 86 (Feb): 160–170. https://doi.org/10.1016/j.cemconcomp.2017.10.010.

Liu, K.-W., A. Baranikumar, Z. Grasley, and A. K. Mukhopadhyay. 2015. "Mechanical properties of alkali-silica reaction gel measured by nano-indenter." *Am. J. Eng. Technol. Soc.* 2 (5): 121.

Lokajíček, T., R. Přikryl, Š. Šachlová, and A. Kuchařová. 2017. "Acoustic emission monitoring of crack formation during alkali silica reactivity accelerated mortar bar test." *Eng. Geol.* 220 (Mar): 175–182.

Mahadevan, S., V. Agarwal, K. Neal, P. Nath, Y. Bao, G. Cai, P. Orme, D. Adams, and D. Kosson. 2016. *A demonstration of concrete structural health monitoring framework for degradation due to alkali-silica reaction*. Idaho Falls, ID: Idaho National Lab.

Mistras-Group. 2014. *Express-8 AE system user manual*. Princeton, NJ: Mistras-Group.

MISTRAS Group. 2011. "PKWDI sensor wideband low power integral preamplifier resonant sensor." Accessed May 22, 2020. https://www.physicalacoustics.com/by-product/sensors/PKWDI-200-1000-kHz-Wideband-Differential-Integral-Preamp-AE-Sensor.

Morenon, P., S. Multon, A. Sellier, E. Grimal, F. Hamon, and E. Bourdarot. 2017. "Impact of stresses and restraints on ASR expansion." *Constr. Build. Mater.* 140 (Jun): 58–74. https://doi.org/10.1016/j.conbuildmat.2017.02.067.

Murtagh, F., and P. Legendre. 2014. "Ward's hierarchical agglomerative clustering method: Which algorithms implement Ward's criterion?" *J. Classification* 31 (3): 274–295. https://doi.org/10.1007/s00357-014-9161-z.

Pan, J., Y. Feng, J. Wang, Q. Sun, C. Zhang, and D. Owen. 2012. "Modeling of alkali-silica reaction in concrete: A review." *Front. Struct. Civ. Eng.* 6 (1): 1–18. https://doi.org/10.1007/s11709-012-0141-2.

Phair, J. W., S. N. Tkachev, M. H. Manghnani, and R. A. Livingston. 2005. "Elastic and structural properties of alkaline-calcium silica hydrogels." *J. Mater. Res.* 20 (2): 344–349. https://doi.org/10.1557/JMR.2005.0061.

Plusquellec, G., M. R. Geiker, J. Lindgård, and K. De Weerdt. 2018. "Determining the free alkali metal content in concrete—Case study of an ASR-affected dam." *Cem. Concr. Res.* 105 (Mar): 111–125. https://doi.org/10.1016/j.cemconres.2018.01.003.

Ponce, J., and O. R. Batic. 2006. "Different manifestations of the alkali-silica reaction in concrete according to the reaction kinetics of the reactive aggregate." *Cem. Concr. Res.* 36 (6): 1148–1156. https://doi.org/10.1016/j.cemconres.2005.12.022.

Pour-Ghaz, M., R. Spragg, J. Castro, and J. Weiss. 2012. "Can acoustic emission be used to detect alkali silica reaction earlier than length change tests." In *Proc., 14th Int. Conf. on Alkali-Aggregate Reaction in Concrete*. Washington, DC: Transportation Research Board.

Rajabipour, F., E. Giannini, C. Dunant, J. H. Ideker, and M. D. Thomas. 2015. "Alkali–silica reaction: Current understanding of the reaction mechanisms and the knowledge gaps." *Cem. Concr. Res.* 76 (Oct): 130–146. https://doi.org/10.1016/j.cemconres.2015.05.024.

Rivard, P., and G. Ballivy. 2005. "Assessment of the expansion related to alkali-silica reaction by the Damage Rating Index method." *Constr.*

Build. Mater. 19 (2): 83–90. https://doi.org/10.1016/j.conbuildmat.2004.06.001.

Rivard, P., G. Ballivy, C. Gravel, and F. Saint-Pierre. 2010. "Monitoring of an hydraulic structure affected by ASR: A case study." *Cem. Concr. Res.* 40 (4): 676–680. https://doi.org/10.1016/j.cemconres.2009.09.010.

Rivard, P., and F. Saint-Pierre. 2009. "Assessing alkali-silica reaction damage to concrete with non-destructive methods: From the lab to the field." *Constr. Build. Mater.* 23 (2): 902–909. https://doi.org/10.1016/j.conbuildmat.2008.04.013.

Sanchez, L., B. Fournier, M. Jolin, and J. Duchesne. 2015. "Reliable quantification of AAR damage through assessment of the Damage Rating Index (DRI)." *Cem. Concr. Res.* 67 (Jan): 74–92. https://doi.org/10.1016/j.cemconres.2014.08.002.

Sanchez, L., B. Fournier, D. Mitchell, and J. Bastien. 2020. "Condition assessment of an ASR-affected overpass after nearly 50 years in service." *Constr. Build. Mater.* 236 (Mar): 117554. https://doi.org/10.1016/j.conbuildmat.2019.117554.

Saouma, V. E., and M. A. Hariri-Ardebili. 2014. "A proposed aging management program for alkali silica reactions in a nuclear power plant." *Nucl. Eng. Des.* 277 (Oct): 248–264. https://doi.org/10.1016/j.nucengdes.2014.06.012.

Saouma, V. E., M. A. Hariri-Ardebili, Y. Le Pape, and R. Balaji. 2016. "Effect of alkali–silica reaction on the shear strength of reinforced concrete structural members. A numerical and statistical study." *Nucl. Eng. Des.* 310 (Dec): 295–310. https://doi.org/10.1016/j.nucengdes.2016.10.012.

Sargolzahi, M., S. A. Kodjo, P. Rivard, and J. Rhazi. 2010. "Effectiveness of nondestructive testing for the evaluation of alkali–silica reaction in concrete." *Constr. Build. Mater.* 24 (8): 1398–1403. https://doi.org/10.1016/j.conbuildmat.2010.01.018.

Schmidt, J. W., S. G. Hansen, R. A. Barbosa, and A. Henriksen. 2014. "Novel shear capacity testing of ASR damaged full scale concrete bridge." *Eng. Struct.* 79 (Nov): 365–374. https://doi.org/10.1016/j.engstruct.2014.08.027.

Seo, J., J. P. Wacker, and L. Duque. 2018. *Evaluating the use of drones for timber bridge inspection*. Madison, WI: Dept. of Agriculture, Forest Service, Forest Products Laboratory.

Sinno, N., and M. H. Shehata. 2019. "Effect of sample geometry and aggregate type on expansion due to alkali-silica reaction." *Constr. Build. Mater.* 209 (Jun): 738–747. https://doi.org/10.1016/j.conbuildmat.2019.03.103.

Smaoui, N., M.-A. Bérubé, B. Fournier, and B. Bissonnette. 2004. "Influence of specimen geometry, orientation of casting plane, and mode of concrete consolidation on expansion due to ASR." *Cem. Concr. Aggregates* 26 (2): 1–13. https://doi.org/10.1520/CCA11927.

Soltangharaei, V., R. Anay, N. Hayes, L. Assi, Y. Le Pape, Z. Ma, and P. Ziehl. 2018. "Damage mechanism evaluation of large-scale concrete structures affected by alkali-silica reaction using acoustic emission." *Appl. Sci.* 8 (11): 2148. https://doi.org/10.3390/app8112148.

Tan, P. N., M. Steinbach, and V. Kumar. 2018. "Introduction to data mining." In *Data mining cluster analysis: Basic concepts and algorithms*. New York: Pearson Education.

Taylor, P., L. Sutter, and J. Weiss. 2012. *Investigation of deterioration of joints in concrete pavements*. InTrans Project 09-361, Iowa DOT TPF-5 (224), DTFH61-06-H-00011 Work Plan 26. Ames, IA: Iowa DOT.

Tcherner, J., and T. Aziz. 2009. "Effects of AAR on seismic assessment of nuclear power plants for life extensions." In *Proc. 20th Int. Conf. on Structural Mechanics in Reactor Technology (SMiRT), Espoo, Finland*, 9–14. Raleigh, NC: International Association for Structural Mechanics in Reactor Technology.

Teramoto, A., M. Watanabe, R. Murakami, and T. Ohkubo. 2018. "Visualization of internal crack growth due to alkali–silica reaction using digital image correlation." *Constr. Build. Mater.* 190 (Nov): 851–860. https://doi.org/10.1016/j.conbuildmat.2018.09.168.

Thomas, M. D. A., K. J. Folliard, B. Fournier, P. Rivard, T. Drimalas, and S. I. Garber. 2013. *Methods for evaluating and treating ASR-affected structures: Results of field application and demonstration projects—Volume II: Details of field applications and analysis*. Washington, DC: USDOT, Federal Highway Administration.

Torkjazi, M., P. S. Mirjafari, and H. Poorzahedy. 2018. "Reliability-based network flow estimation with day-to-day variation: A model validation on real large-scale urban networks." *J. Intell. Transp. Syst.* 22 (2): 121–143. https://doi.org/10.1080/15472450.2017.1413555.

Van Steen, C., L. Pahlavan, M. Wevers, and E. Verstrynge. 2019. "Localisation and characterisation of corrosion damage in reinforced concrete by means of acoustic emission and X-ray computed tomography." *Constr. Build. Mater.* 197 (Feb): 21–29. https://doi.org/10.1016/j.conbuildmat.2018.11.159.

Villeneuve, V., B. Fournier, and J. Duchesne. 2012. "Determination of the damage in concrete affected by ASR—The damage rating index (DRI)." In *Proc., 14th Int. Conf. on Alkali-Aggregate Reaction (ICAAR)*. Washington, DC: Transportation Research Board.

Weise, F., K. Voland, S. Pirskawetz, and D. Meinel. 2012. "Innovative measurement techniques for characterising internal damage processes in concrete due to ASR." In *Proc., Int. Conf. on Alkali Aggregate Reaction (ICAAR)*, 20–25. Austin, TX: Univ. of Texas.

Yang, C.-H., M.-C. Wen, Y.-C. Chen, and S.-C. Kang. 2015. "An optimized unmanned aerial system for bridge inspection." In *Proc., Int. Symp. on Automation and Robotics in Construction, ISARC*, 1. Pittsburgh: International Association for Automation and Robotics in Construction.

Zink, J., and B. Lovelace. 2015. *Unmanned aerial vehicle bridge inspection demonstration project*. St. Paul, MN: Minnesota DOT, Office of Transportation System Management.